Electrochemistry
The Electrochemical Society of Japan
Received: March 28, 2023
Accepted: April 24, 2023
Published online: April 26, 2023
Issued: October 5, 2023
https://doi.org/10.5796/electrochemistry.23-00032
Comprehensive Paper (Invited Paper) *Electrochemistry*, **91(10)**, 102004 (2023)

Young Researcher Award of The Electrochemical Society of Japan (Sano Award), 2022

Development of Electrode Materials Based on Design Guideline of Electronic Structure Obtained by Synchrotron Radiation X-ray Analyses

Kentaro YAMAMOTO*,†,§

Graduate School of Human and Environmental Studies, Kyoto University, Yoshida-nihonmatsu-cho, Sakyo, Kyoto 606-8501, Japan

* *Corresponding author: k.yamamoto@cc.nara-wu.ac.jp*

ABSTRACT

Electrode reactions in electrochemical devices often consist of charge transfer at electrode/electrolyte interface and charge compensation in electrode active material. Therefore, to design electrochemical devices with high electrochemical performance, it is important to understand electronic structures of the electrode/electrolyte interface and electrode bulk during electrochemical reactions, and to design electrode materials to control them. In this paper, certain phenomena at the electrode/electrolyte interface and electrode bulk in lithium-ion batteries are clarified by using synchrotron radiation X-ray analyses. The information obtained from those X-ray analyses are applied to control the structure of the electrode/electrolyte interface and electrode bulk. Moreover, new cathode materials for all-solid-state fluoride-ion with high power and cyclic performances have been developed, compared to simple metal/metal fluoride materials, by using the findings obtained from the synchrotron radiation X-ray analyses.

Keywords : Electronic Structure, Synchrotron Radiation X-ray Analysis, Lithium-ion Battery, All-solid-state Fluoride-ion Battery

1. Introduction

Electrochemical devices such as lithium-ion batteries (LIBs), post-lithium-ion batteries, and polymer electrolyte fuel cells are expected to be widely used as energy storage media in electric vehicles and smart grids to solve the environmental and energy problems.[1] Electrode reactions in the electrochemical devices often consist of charge transfer at the electrode/electrolyte interface and charge compensation associated with carrier ion transfer in the electrode active material. For example, in LIBs, lithium-ions are inserted into and extracted from the electrode active material at the electrode/electrolyte interface, and electron transfer occurs simultaneously. In addition, charge compensation occurs in the electrode active material when lithium-ions move. Therefore, in order to improve performances of the electrochemical devices, it is necessary to understand electronic structures of the electrode/electrolyte interface and electrode bulk during electrochemical reactions, and to design electrode materials to control them. This paper reviews synchrotron radiation X-ray analyses suitable for examining the respective phenomena at the electrode/electrolyte interface and electrode bulk. In addition, it describes new electrode materials using the electronic structural material design guidelines obtained from those analyses.

Kentaro Yamamoto (Associate Professor, Faculty Engineering, Nara Women's University)

Kentaro Yamamoto received Ph.D from, Kyoto University in 2015. He worked as a research assistant professor in Kyusyu University (2015–2016), as research an assistant professor and an associate professor in Kyoto University (2016–2022). Then he worked as an associate professor in Nara Women's University from 2022. His research interests are development of electrode and electrolyte materials for rechargeable batteries.

1) Interfacial electronic structure between electrode and electrolyte

In LIBs, the interface between electrode and electrolyte is the starting point for the whole electrochemical reactions.[2] Because the electrode and electrolyte each have different inner potentials, potential compensation occurs at the electrode/electrolyte interface. The potential compensation forms a space-charge layer on the electrode side and an electric double layer on the electrolyte side, resulting in the electronic structure at the interface that is different from the bulk. As in LIBs, the space charge layer's structure is expected to be responsible for the cyclability and power density, clarifying and controlling the interfacial structure are important for improving the electrochemical performances.[3] However, elucidating the space charge layer's structure is difficult because the following three conditions must be met: (1) A smooth electrode/electrolyte model interface must be constructed to extract information only from the interface; (2) Analysis under battery operating conditions (*operando*) is essential; (3) The thickness of the space-charge layer is speculated to be on the order of a few nanometers, so analytical methods with a similar level of spatial resolution are necessary. The electrode of LIB is usually a composite electrode, which is a mixture of active material, carbon, and binder. Complex three-dimensional morphology of the composite electrode makes it difficult to extract information on the electrode/electrolyte interface. Therefore, it is appropriate to use a thin-film electrode that can define the interface to analyze the electrode/electrolyte interfacial structure. It has been reported that surface X-ray diffraction[4] and X-ray reflectometry[5] for thin-film electrodes are applied to analyze the electrode/electrolyte

†Present address: Faculty of Engineering, Nara Women's University, Kitauoya-nishimachi, Nara 630-8263, Japan
§ECSJ Active Member
K. Yamamoto orcid.org/0000-0002-8739-4246

interface structure on *operando* conditions. Although these methods provide useful information about the interfacial structure, they have disadvantage for the analysis of amorphous and electronic structures. *Operando* total reflection fluorescence X-ray absorption spectroscopy (TRF-XAS) is a powerful tool for the analysis of amorphous and electronic structures at the electrode/electrolyte interface under operating conditions.[6,7] In this section, clarifications of phenomena at the cathode/electrolyte interface in LIBs using TRF-XAS are introduced.

Because the refractive index of X-ray is slightly less than 1, a highly collimated incident X-ray beam on a smooth interface at an angle smaller than the critical angle will be totally reflected.[8] Under such a condition, the X-ray beam penetrates only a few nanometers from the sample surface and makes atoms on the electrode surface excite, providing only the surficial information. Considering the density of $LiCoO_2$ and the energy of X-ray absorption spectroscopy for Co *K*-edge, the calculated total reflection angle of $LiCoO_2$ is 0.28°, and the penetration depth of X-ray at that angle is estimated to be 6.8 nm. When the incident X-ray angle is set to 0.2°, the penetration depth of X-ray is estimated to be ~3 nm. When the incident angle the X-ray is larger than the total reflection angle, the penetration depth of the X-ray is estimated to be approximately 100 nm, which means that the entire film, i.e., the bulk information, can be obtained when the $LiCoO_2$ thin-film with 50 nm thickness is used.

Figure 1 shows XANES spectra for Co *K*-edge and Fe *K*-edge of the surface of the $LiCoO_2$ and $LiFePO_4$ thin-film electrodes before and after liquid organic electrolyte immersion, which are obtained by using the *operando* TRF-XAS.[7] In the $LiCoO_2$ thin-film electrode, the energy of the absorption edge shifts to the lower energy side after the electrolyte immersion, meaning that the Co ions at the $LiCoO_2$ surface is reduced by contact with the electrolyte (Fig. 1a). On the other hand, in the $LiFePO_4$ thin-film electrode, energy shift of the absorption edge to lower is not observed after the electrolyte immersion, meaning that the Fe ions at the $LiFePO_4$ surface is not reduced by contact with the electrolyte (Fig. 1b). Figure 2 shows the absorption energy at normalized intensity of 0.5 obtained from the XANES spectra of the surface and bulk for the $LiCoO_2$ and $LiFePO_4$ thin-film electrodes during charge/discharge processes. In the $LiCoO_2$ bulk, the absorption energy shifts to the higher energy side with increasing voltage, and then returns back to the original energy with decreasing voltage (Fig. 2a). This means that the redox of Co ions in the bulk is reversible during charge/discharge processes. On the $LiCoO_2$ surface, although the absorption energy shifts to the higher energy side with increasing voltage, it does not return back to the original energy with decreasing voltage. This means that the redox of Co ions on the surface is irreversible during charge/discharge processes, in contrast to the bulk. On the other hand, in the case of the $LiFePO_4$ thin-film electrode, the absorption energy of both of the surface and bulk XANES spectra shifts to the higher energy side with increasing voltage. Then it returns back to the original energy with decreasing voltage (Fig. 2b). This means that the redox of Fe ions of both of the surface and bulk for the $LiFePO_4$ thin-film electrode is reversible during charge/discharge processes, in contrast to the $LiCoO_2$ thin-film electrode.

The reduction of Co ions at the $LiCoO_2$ surface is attributed to formation of a space charge layer (Fig. 3a). The energy level of the bottom of the conduction band in $LiCoO_2$ is sufficiently low to allow electron transfer from the electrolyte to the electrode because of its relatively small band gap of ~1.5 eV.[9] The formation of the space charge layer causes irreversible lithium-ions extraction/insertion reactions, which is the origin of the $LiCoO_2$ electrode deterioration. During further cycling, the irreversible layers continue to grow from

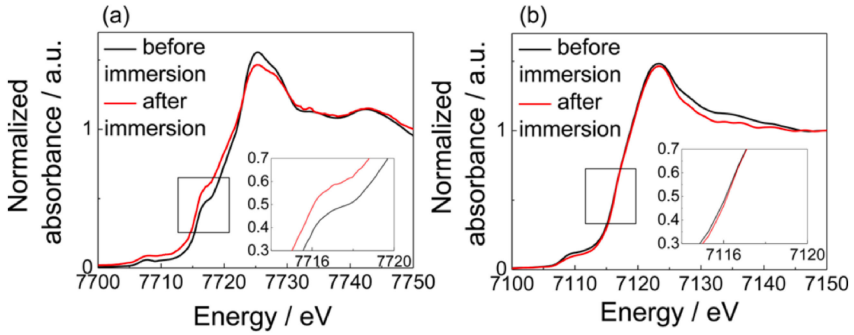

Figure 1. (a) Co *K*-edge surface and XANES spectra of $LiCoO_2$ and (b) Fe *K*-edge surface XANES spectra of $LiFePO_4$ before (black line) and after (red line) electrolyte immersion, obtained via *operando* TRF-XAS. Reproduced with permission from Ref. 7. Copyright 2014 American Chemical Society.

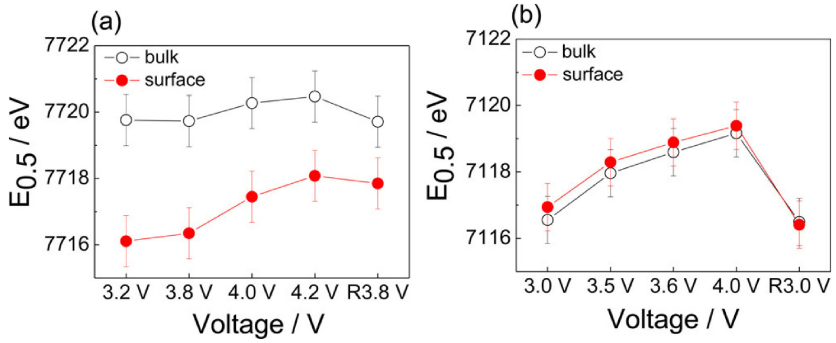

Figure 2. $E_{0.5}$ values of (a) Co *K*-edge surface (red) and bulk (white) XANES spectra of the $LiCoO_2$ electrode and (b) Fe *K*-edge surface (red) and bulk (white) XANES spectra of the $LiFePO_4$ electrode during lithium-ion extraction and insertion. (R3.8 V and R3.0 V are the applied voltages during the lithium-ion insertion process. Error bars are calculated using the accuracy of the incident X-ray energy (0.01 %).) Reproduced with permission from Ref. 7. Copyright 2014 American Chemical Society.

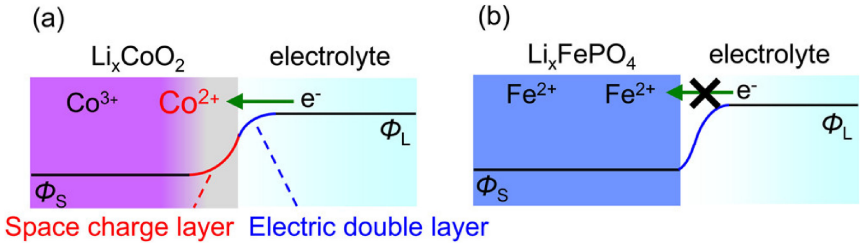

Figure 3. Schematic illustrations of the changes in the electronic structure at the (a) $LiCoO_2$/electrolyte and (b) $LiFePO_4$/electrolyte interfaces upon electrolyte immersion. (Φ_S and Φ_L are the inner potentials of the electrode and electrolyte, respectively. To simplify, it is assumed that the plane of polycrystalline $LiCoO_2$ and $LiFePO_4$ facing the electrolyte is perpendicular to (001) and parallel to (010), respectively.) Reproduced with permission from Ref. 7. Copyright 2014 American Chemical Society.

the surface to the bulk, and the discharge capacity fades. In contrast to the situation in $LiCoO_2$, the reduction of Fe ions on the $LiFePO_4$ surface does not occurs with the electrolyte immersion, indicating that a potential change inside a space charge layer in the $LiFePO_4$ surface is not large. Because of a wider band gap (~3.7 eV) of $LiFePO_4$[10,11] than that of $LiCoO_2$, the bottom of the conduction band energy level of $LiFePO_4$ would be higher than that of $LiCoO_2$, impeding electron transfer from the electrolyte to the $LiFePO_4$ surface. Therefore, the potential change in the space charge layer in $LiFePO_4$ is smaller than that in $LiCoO_2$, and the potential gap between the $LiFePO_4$ electrode and electrolyte is compensated mainly by an electrical double layer in the electrolyte (Fig. 3b). The lack of a large potential change in the space charge layer at the $LiFePO_4$ surface is the origin of the stable behavior with electrolyte contact and during lithium-ions extraction/insertion reactions.

To suppress the reaction on the electrode surface by contact with the electrolyte, surface coating with oxides such as MgO has been examined as an interfacial modification approach from the electrode side.[12] The surface coating layer suppresses the formation of the space charge layer on the $LiCoO_2$ surface and also stabilizes the layered structure by acting as a pillar at high potentials, resulting in improvement of cyclability at high potentials. The use of additives such as vinylene carbonate (VC) has been investigated as another interfacial modification approach from the electrolyte side:[13] solid electrolyte interphase formed on the electrode surface by decomposition of VC stabilizes the $LiCoO_2$ electrode surface, resulting in improvement of cyclability. The use of *operando* TRF-XAS has revealed the correlation between the electrode/electrolyte interfacial structure and the electrochemical properties.

2) Charge compensation mechanism of Li-excess metal oxide cathodes

In electrode reactions of energy storage devices, the capacity is defined by the charge compensation of the electrode material with carrier ions insertion/extraction reactions. Therefore, it is important to elucidate and control the electronic structure of the electrode material. In LIBs, many researches on the elucidation and control of the electronic structure of electrode materials have been conducted vigorously, focusing on transition metal ions. However, the development of electrode materials by controlling transition metal ions is reaching its limits. Therefore, in recent years, Li-excess metal oxides that utilize the charge compensation of oxide ions as well as transition metal ions have attracted attention as cathode materials that exhibit high capacity.[14] However, the charge compensation by oxide ions can cause irreversible oxygen loss[15] and phase transitions.[16] In order to suppress these phenomena, it is necessary to design materials based on an understanding of the electronic state of oxide ions during charge process. In this section, the studies on the electronic structure of oxide ions in Li-excess metal oxide cathodes during charge process and their electronic structure control are described.

Li-excess metal oxide $Li_{1.2}Ti_{0.4}Mn_{0.4}O_2$ with disorder rock-salt structure[17] is used as a model cathode to obtain high reversible capacity. As shown in Fig. 4a, the $Li_{1.2}Ti_{0.4}Mn_{0.4}O_2$ has a charge capacity of 381 mAh g^{-1} with a voltage slope up to $x = 0.4$ and a voltage plateau of 4.2 V, and a capacity of 306 mAh g^{-1} during discharge.[18] In the charge process, the partial pressure increase of O_2 gas is not observed for the $Li_{1.2}Ti_{0.4}Mn_{0.4}O_2$ (Fig. 4b) via an online mass electrochemical mass spectrometry, indicating the possibility of no oxygen loss in this system. The electronic structures of

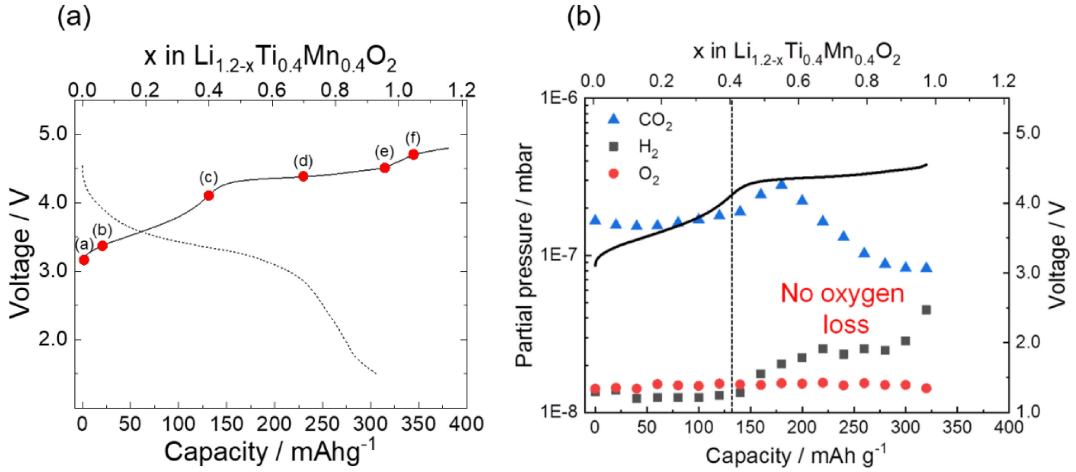

Figure 4. (a) Charge and discharge profiles for $Li_{1.2}Ti_{0.4}Mn_{0.4}O_2$ at 1/20 C at 55 °C. *Operando* soft XAS measurements are performed at different states of charge, corresponding to the points on the charge curves. (b) CO_2, H_2, and O_2 partial gas pressures of $Li_{1.2}Ti_{0.4}Mn_{0.4}O_2$ as a function of the state of charge by using online electrochemical mass spectrometry. Reproduced with permission from Ref. 18. Copyright 2020 American Chemical Society.

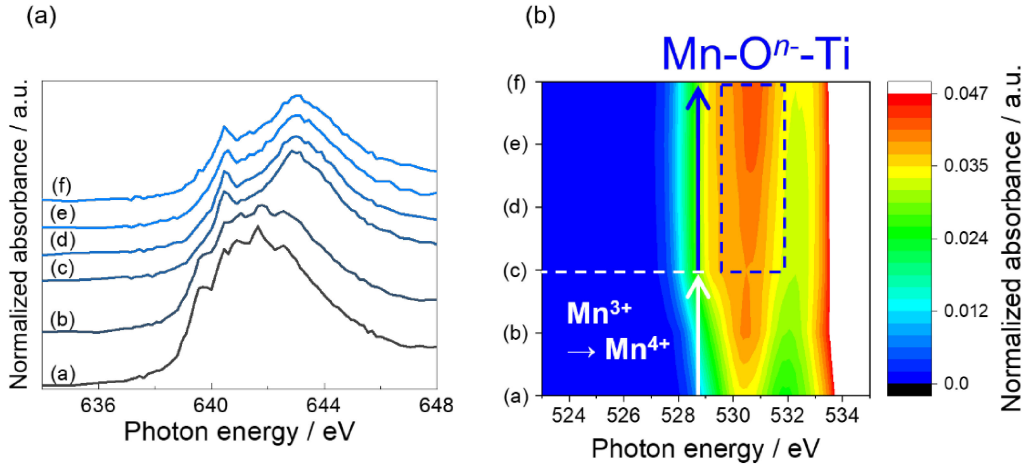

Figure 5. (a) Mn *L*-edge and (b) O *K*-edge XAS spectra of $Li_{1.2}Ti_{0.4}Mn_{0.4}O_2$ obtained by using *operando* soft XAS at different states of charge in partial fluorescence mode, corresponding to the points on the charge curves in Fig. 4a. Reproduced with permission from Ref. 18. Copyright 2020 American Chemical Society.

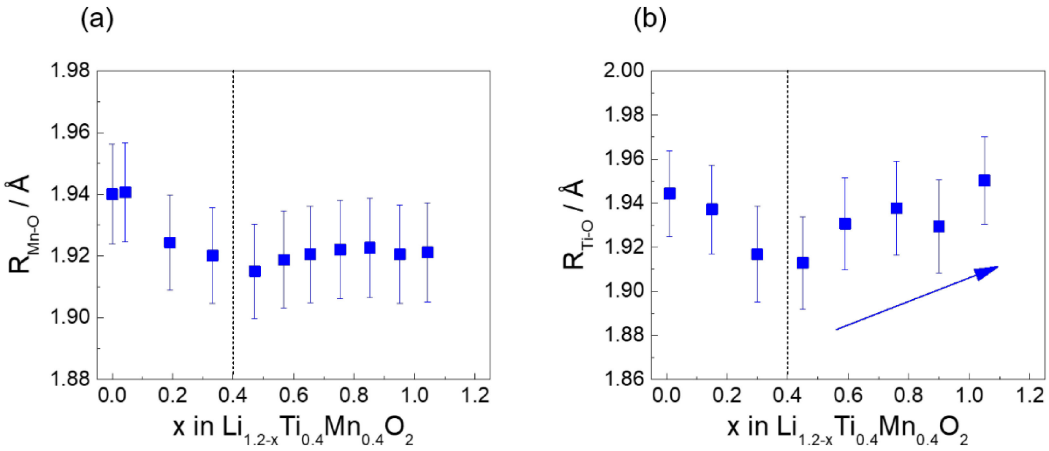

Figure 6. (a) Mn–O and (b) Ti–O distances of $Li_{1.2}Ti_{0.4}Mn_{0.4}O_2$ as a function of the state of charge by using *operando* EXAFS analysis. Reproduced with permission from Ref. 18. Copyright 2020 American Chemical Society.

transition metal ions and oxide ions for the $Li_{1.2}Ti_{0.4}Mn_{0.4}O_2$ during charge process are examined by using *operando* soft X-ray absorption spectroscopy (soft XAS). Figure 5 shows XAS spectra of Mn *L*-edge and O *K*-edge obtained by the *operando* soft XAS at points (a)–(f) in Fig. 4a. In the XAS spectrum for Mn L_{III}-edge, a board peak is observed at ~641.5 eV before the charge process (Fig. 5a). The broad peak is separated into two peaks and shifted to a higher energy side in the slope region ((a) to (c) in Fig. 4a) during the charge process. This change means the Mn ions are oxidized from Mn^{3+} to Mn^{4+} state. In the subsequent charge process ((c) to (f) in Fig. 4a), the two peaks are unchanged, meaning that the Mn ions are not oxidized and responsible for the charge compensation. In the XAS spectrum for O *K*-edge, a board peak, which is attributed to the transitions from the O 1*s* level to the hybridized states of the Mn 3d and O 2p orbitals,[19] is observed at ~530.4 eV before the charge process (Fig. 5b). The intensity at 529.5 eV is increased in the slope region ((a) to (c) in Fig. 4a) during the charge process. This change is attributed to the spin multiplicity and crystal field effect with the oxidation of the Mn ions from Mn^{3+} to Mn^{4+}, as observed in the Mn-L_{III} XAS spectra (Fig. 5a). In the subsequent charge process ((c) to (f) in Fig. 4a), intensity of the peak at 530.7 eV is increased. Because the Mn ions are not oxidized in the late charge process as observed in the Mn-L_{III} XAS spectra (Fig. 5a), the peak intensity increase is attributed to oxidation of oxide ions. Local structures around transition metal ions for the $Li_{1.2}Ti_{0.4}Mn_{0.4}O_2$ during charge process are examined by using *operando* XAS. Figure 6 shows Mn-O and Ti-O distances obtained from the extended X-ray absorption fine structure (EXAFS) analysis for the Mn and Ti *K*-edge XAS spectra. The Mn-O distance is decreased in the region $x = 0$–0.4 and remained constant from $x = 0.4$–1.1 (Fig. 6a), corresponding to the oxidation of Mn ions as observed in the Mn-L_{III} XAS spectra (Fig. 5a). On the other hand, the Ti–O distances is decreased in the region $x = 0$–0.4 and gradually increased from $x = 0.4$–1.1 (Fig. 6b). These results indicate that the holes created by oxidation at the late charge process are localized around the Ti ions and the presence of the Ti ions stabilizes the oxidation of oxide ions. The oxidation of the oxide ions around the Ti ions weakens the coulombic interaction between the Ti and oxide ions, resulting in the increase in the Ti–O distances. A more detailed analysis of the electronic structure for the $Li_{1.2}Ti_{0.4}Mn_{0.4}O_2$ using high-energy X-ray Compton scattering has revealed that the holes are formed in the isolated oxygen 2p orbitals due to the weak π-bonding property caused by electrostatic repulsion between the transition metal t_{2g} orbital and the oxygen 2p orbital.[20] A similar mechanism is proposed for $Li_{1.2}Ni_{0.13}Co_{0.13}Mn_{0.54}O_2$, in which hole localization on the oxide ions coordinated with Mn^{4+} and Li^+ is promoted.[21] The relatively higher ionic character of the $Li_{1.2}Ti_{0.4}Mn_{0.4}O_2$ enhances the hole local-

ization with Ti^{4+}, resulting in the stabilized oxide ions' redox and the high reversible capacity.

Considering energy of nitrogen 2p orbital is higher than that of oxygen 2p orbital, the hole formation during charge process can occur in not only oxygen 2p orbitals but also nitrogen 2p orbitals. Therefore, nitrogen doping can be a strategy to improve the capacity of the oxide ions' redox in Li-excess metal oxide cathode. It has been reported that nitrogen-doped $Li_{1.2}Ti_{0.4}Mn_{0.4}O_2$ with optimized composition, $Li_{1.2}Ti_{0.4}Mn_{0.4}O_{1.85}N_{0.10}$, provides a higher capacity than non-doped $Li_{1.2}Ti_{0.4}Mn_{0.4}O_2$ because of an effective reduction of Mn and stabilization of the hole formation in oxide ions during charge process.[22] Therefore, in order to achieve high capacity by using anionic redox of Li-excess metal oxide cathodes, it is important to enhance electron localization on anions in the structure.

3) Development of electrode materials for all-solid-state fluoride-ion batteries

LIBs are widely used in human society because of their high energy density, high power density, and long-term durability. As mentioned in the previous section, in recent years, the cathode materials by using oxide ions' redox in addition to transition metal ions' redox have been developed to improve the energy density. However, as the need for longer range electric vehicles and for grid storage is increasing, it is necessary to develop batteries with even higher capacity and that do not rely on lithium. To meet these demands, batteries using different carrier ions (Na^+, Mg^{2+}, Ca^{2+}, Cl^-, F^-, etc.) have been proposed.

Among these, all-solid-state fluoride-ion batteries that use fluoride-ions as carriers[23] have been attracting attention as a storage battery with high energy density that theoretically exceeds that of LIBs. The all-solid-state fluoride-ion batteries can achieve high capacity by utilizing multi-electron reactions in metal fluorides such as CuF_2 with monovalent fluoride ions as carriers. It has been reported that the electrode/electrolyte interface reaction rate depends on the ionic conductivity of the solid electrolyte in all-solid-state fluoride-ion batteries.[24] This indicates that the power density equivalent to that of all-solid-state LIBs may be achieved by using fluoride-ion conductors with high ionic conductivity. Therefore, the all-solid-state fluoride-ion batteries are expected to be as next-generation batteries with high energy density and high power density. However, when simple metals/metal fluorides are used, the power density and cyclability are poor due to the rapid decrease in ionic and electronic conductivities and large volume change during charge/discharge, i.e., fluorination/defluorination processes. To solve these issues, use of various metals/metal fluorides,[25] mitigation of volume change of metals/metal fluorides during charge/discharge processes by alloying,[26] and nanocomposites of metals/metal fluorides and solid electrolytes have been studied.[27] Although these methods have some effect on improving the power density and cyclability of the metals/metal fluorides electrodes in all-solid-state fluoride-ion batteries, they have not led to dramatic improvements. Therefore, in order to use metals/metal fluorides as electrodes, further studies improving for the electrochemical properties are needed. This section introduces researches that use metal oxides as similar to electrode materials applied in LIBs as a different approach from those described above to solve the issues of power density and cyclability of all-solid-state fluoride-ion battery cathodes.

Figure 7a shows the charge/discharge curves when a metal oxide Cu_2O was applied as the cathode of all-solid-state fluoride-ion battery.[28] The Cu_2O cathode provides a charge capacity of 314 mAh g^{-1} and a discharge capacity of 220 mAh g^{-1} in the initial charge and discharge processes at 0.02 C (1 C = 375 mA g^{-1}), respectively, and a reversible capacity of 134 mAh g^{-1} after 30 cycles. Figure 7b compares the rate performance of the Cu_2O and Cu thin-film cathodes. Even though the electrochemical measurement of the Cu thin-film cathode is performed with a thin-film three-electrode cell, whereas that of the Cu_2O cathode is performed with a bulk-type cell, the rate performance of the Cu_2O cathode is superior to the Cu thin-film cathode. The average particle size of the Cu_2O cathode is approximately 50–60 nm, indicating that the diffusion length of fluoride-ions in the Cu_2O cathode is greater than that of fluoride-ions in the Cu thin-film cathode with 10 nm thickness. These results suggest that the fluoride/defluorination reactions in the Cu_2O cathode are kinetically superior to those in the Cu cathode. The apparent diffusion coefficient of fluoride-ions in Cu_2O cathode is 10^{-11} to 10^{-10} cm^2 s^{-1} (Fig. 7c), which is determined by potentiostatic intermittent titration technique. This value is comparable to that of the cathode materials for LIBs at room temperature.[29–33] These results indicate that high-power all-solid-state fluoride-ion battery cathodes can be developed by using metal oxides. However, synchrotron X-ray diffraction (XRD) and EXAFS analysis of Cu *K*-edge XAS have revealed that the rapid capacity drop in Cu_2O cathode in the first few cycles is due to irreversible amorphization of the Cu_2O cathode after charge process. To suppress the capacity drop, it is necessary to design the metal oxides in which amorphization does not occur during charge/discharge processes.

One approach to suppress the capacity loss due to amorphization of cathode materials is to use the cathode materials that undergo topotactic fluoride-ions intercalation/deintercalation reactions. It has been reported that compounds with perovskite analogous structures

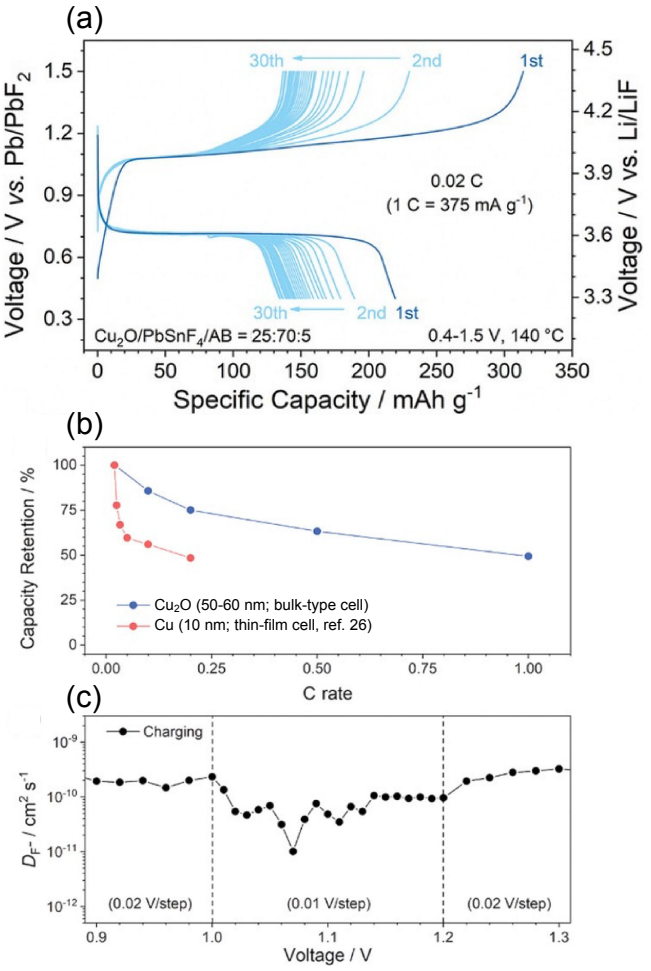

Figure 7. (a) Charge/discharge profiles of Cu_2O cathode for cycles 1–30 at 140 °C at 0.02 C. (b) Comparisons of rate capabilities of Cu_2O bulk and a Cu thin-film system from Ref. 26. (c) Apparent fluoride ions diffusion coefficients (D_{F-}) calculated from potentiostatic intermittent titration technique. Reproduced from Ref. 28 with permission. Copyright 2021, Wiley-VCH.

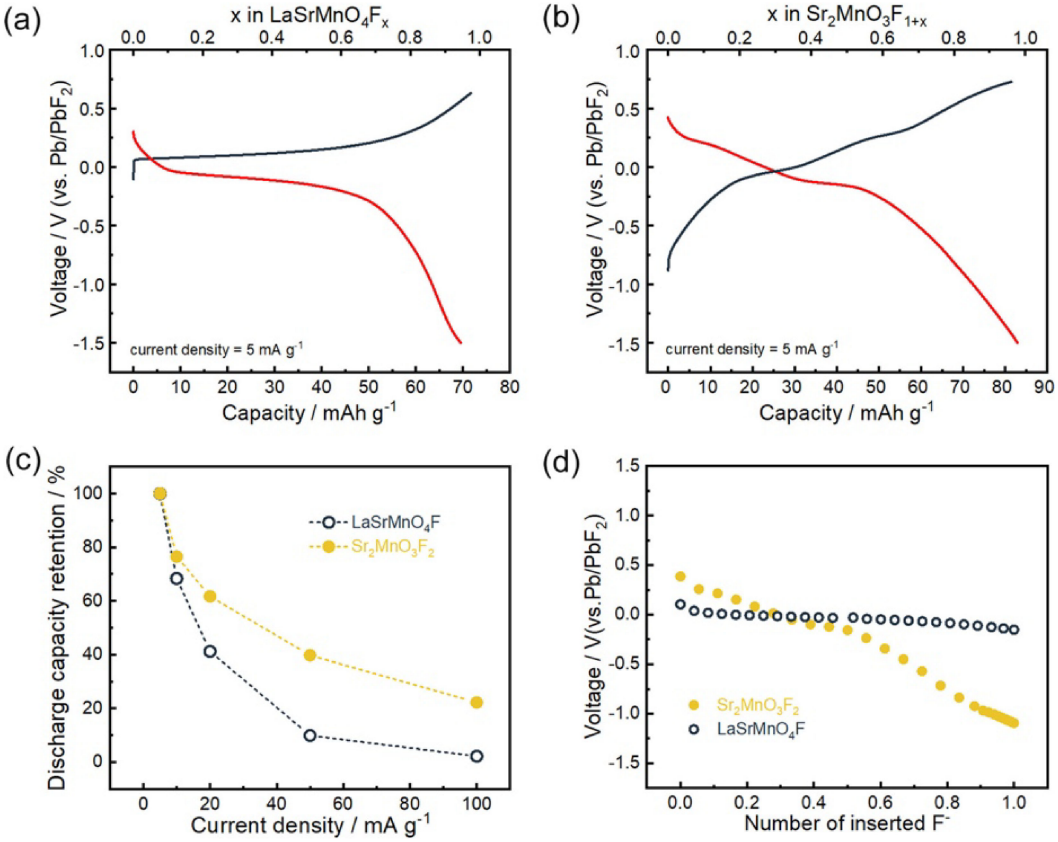

Figure 8. Electrochemical performances of $LaSrMnO_4F$ and $Sr_2MnO_3F_2$. Discharge/charge profiles of (a) $LaSrMnO_4F$ and (b) $Sr_2MnO_3F_2$. (c) Rate performance of discharge capacity retentions of the two active materials; the capacity is normalized for more intuitive comparison. (d) OCVs at various fluorine contents. Reproduced with permission from Ref. 35. Copyright 2022 American Chemical Society.

exhibit intercalation/deintercalation reactions of fluoride-ions.[34,35] Figures 8a and 8b show the charge/discharge curves of $LaSrMnO_4F$ and $Sr_2MnO_3F_2$ cathodes synthesized by chemical fluorination of $LaSrMnO_4$ and Sr_2MnO_3F with perovskite analogous structures.[35] The $LaSrMnO_4F$ cathode provides a discharge capacity of 70 mAh g^{-1} and a charge capacity of 72 mAh g^{-1}, whereas the $Sr_2MnO_3F_2$ cathode exhibits a discharge capacity of 84 mAh g^{-1} and a charge capacity of 83 mAh g^{-1}. The both cathodes show a reversible capacity. The $Sr_2MnO_3F_2$ cathode shows better capacity retention at higher current densities than the $LaSrMnO_4F$ cathode (Fig. 8c). The $LaSrMnO_4F$ exhibits a flat open-circuit-voltage (OCV) over a wide range of fluorine content, as seen in the $LiFePO_4$ cathode of LIBs,[29] whereas the OCV of the $Sr_2MnO_3F_2$ gradually changes with fluorine content (Fig. 8d). By combining the OCV results with XAS and synchrotron XRD measurements, it has been found that the fluoride-ions insertion into the $LaSrMnO_4$ proceeds by a two-phase reaction and that into the Sr_2MnO_3F proceeds by a solid solution reaction (Fig. 9). The volume expansion of the $LaSrMnO_4$ during fluoride-ions insertion is relatively large (6.22 %) while that of the Sr_2MnO_3F is relatively small (3.08 %). In the Sr_2MnO_3F, because 50 % of the apical site is replaced by fluoride-ion and the electrostatic repulsion between the anion of the apical site and the inserted fluoride-ion is relatively small. This results in a smaller volume change during charging and higher power density, compared to the $LaSrMnO_4$. The finding that the power density can be improved by controlling the anion of apical site is useful information for the development of cathodes for all-solid-state fluoride ion batteries.

4) Summary and Outlook

This paper introduces the author's studies on the electronic structure of the cathode/electrolyte interface and the charge compensation mechanism of the Li-excess metal oxide cathodes in LIBs using synchrotron radiation X-ray analysis techniques, and material design based on the knowledge obtained from these studies. The cyclability and stability at high potential of LIB cathodes can be improved by controlling the specific electronic structure of the cathode/electrolyte interface, which is different from that of the bulk. In addition, the reversible anion redox can be utilized by localizing electrons on 2p orbitals of anions in the Li-excess metal oxide cathodes to obtain high capacity. By using these obtained findings to develop all-solid-state fluoride-ion battery materials, it is found that all-solid-state fluoride-ion battery with high power and cyclic performances can be realized by using the intercalation-type oxyfluoride cathode materials compared to the simple metal/metal fluoride materials. Although the intercalation-type cathode materials have the problem of small capacity, there is a possibility that higher capacity can be achieved by utilizing the anion redox and other knowledges obtained from LIB cathodes, and further development is expected in the future.

Acknowledgments

The author would like to acknowledge Prof. Yoshiharu Uchimoto, Prof. Yuki Orikasa, Prof. Koji Nakanishi, Prof. Toshiyuki Matsunaga, Prof. Hiroshi Kageyama, Prof. Naoaki Yabuuchi, Dr. Daiko Takamatsu, Dr. Hajime Tanida, and members in Uchimoto laboratory for their supervision, discussion, technical advices and experimental efforts. This work was supported by the RISING project of NEDO (Grant Number JPNP09012), the ALCA-SPRING project of JST (Grant Number JPMJAL1301), the Mirai Program of JST (Grant Number JPMJMI18E2) and JSPS Grant-in-Aid for Scientific Research on Innovative Areas ("Mixed-Anion", Grant Number JP16H6441).

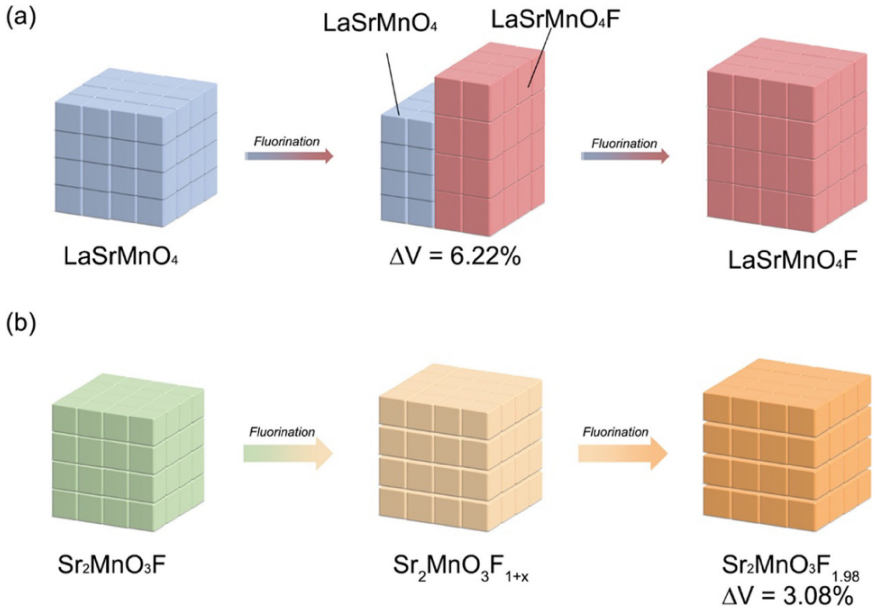

Figure 9. Schematic illustration of the volume changes and phase transition models during the charging process for (a) $LaSrMnO_4F$ and (b) $Sr_2MnO_3F_2$. Reproduced with permission from Ref. 35. Copyright 2022 American Chemical Society.

CRediT Authorship Contribution Statement

Kentaro Yamamoto: Writing – original draft (Lead)

Conflict of Interest

The authors declare no conflict of interest in the manuscript.

Funding

The RISING project of NEDO: JPNP09012
The ALCA-SPRING project of JST: JPMJAL1301
The Mirai Program of JST: JPMJMI18E2
JSPS Grant-in-Aid for Scientific Research on Innovative Areas: JP16H6441

References

1. M. Armand and J. M. Tarascon, *Nature*, **451**, 652 (2008).
2. Z. Ogumi, *Electrochemistry*, **78**, 319 (2010).
3. K. Xu and A. von Cresce, *J. Mater. Chem.*, **21**, 9849 (2011).
4. K. Sakamoto, M. Hirayama, N. Sonoyama, D. Mori, A. Yamada, K. Tamura, J. Mizuki, and R. Kanno, *Chem. Mater.*, **21**, 2632 (2009).
5. M. Hirayama, N. Sonoyama, T. Abe, M. Minoura, M. Ito, D. Mori, A. Yamada, R. Kanno, T. Terashima, M. Takano, K. Tamura, and J. Mizuki, *J. Power Sources*, **168**, 493 (2007).
6. D. Takamatsu, Y. Koyama, Y. Orikasa, S. Mori, T. Nakatsutsumi, T. Hirano, H. Tanida, H. Arai, Y. Uchimoto, and Z. Ogumi, *Angew. Chem., Int. Ed.*, **51**, 11597 (2012).
7. K. Yamamoto, T. Minato, S. Mori, D. Takamatsu, Y. Orikasa, H. Tanida, K. Nakanishi, H. Murayama, T. Masese, T. Mori, H. Arai, K. Yukinori, Z. Ogumi, and Y. Uchimoto, *J. Phys. Chem. C*, **118**, 9538 (2014).
8. H. Saisho and Y. Gohshi, *Applications of Synchrotron Radiation to Materials Analysis*, Elsevier Science B. V., Amsterdam (1996).
9. A. Juhin, F. de Groot, G. Vanko, M. Calandra, and C. Brouder, *Phys. Rev. B*, **81**, 115115 (2010).
10. A. Yamada and S.-C. Chung, *J. Electrochem. Soc.*, **148**, A960 (2001).
11. F. Zhou, K. Kang, T. Maxisch, G. Ceder, and D. Morgan, *Solid State Commun.*, **132**, 181 (2004).
12. K. Yamamoto, Y. Orikasa, D. Takamatsu, Y. Koyama, S. Mori, T. Masese, T. Mori, T. Minato, H. Tanida, T. Uruga, Z. Ogumi, and Y. Uchimoto, *Electrochemistry*, **82**, 891 (2014).
13. D. Takamatsu, Y. Orikasa, S. Mori, T. Nakatsutsumi, K. Yamamoto, T. Minanto, Y. Koyama, T. Hirano, H. Tanida, H. Arai, Y. Uchimoto, and Z. Ogumi, *J. Phys. Chem. C*, **119**, 9791 (2015).
14. M. Sathiya, G. Rousse, K. Ramesha, C. P. Laisa, H. Vezin, M. T. Sougrati, M.-L. Doublet, D. Foix, D. Gonbeau, W. Walker, A. S. Prakash, M. Hassine, L. Ben Dupont, and J.-M. Tarascon, *Nat. Mater.*, **12**, 827 (2013).
15. A. R. Armstrong, M. Holzapfel, P. Novák, C. S. Johnson, S.-H. Kang, M. M. Thackeray, and P. G. Bruce, *J. Am. Chem. Soc.*, **128**, 8694 (2006).
16. N. Yabuuchi, K. Yoshii, S.-T. Myung, I. Nakai, and S. Komaba, *J. Am. Chem. Soc.*, **133**, 4404 (2011).
17. N. Yabuuchi, M. Nakayama, M. Takeuchi, S. Komaba, Y. Hashimoto, T. Mukai, H. Shiiba, K. Sato, Y. Kobayashi, A. Nakao, M. Yonemura, K. Yamanaka, K. Mitsuhara, and T. Ohta, *Nat. Commun.*, **7**, 13814 (2016).
18. K. Yamamoto, Y. Zhou, N. Yabuuchi, K. Nakanishi, T. Yoshinari, T. Kobayashi, Y. Kobayashi, R. Yamamoto, A. Watanabe, Y. Orikasa, K. Tsuruta, J. Park, H. R. Byon, Y. Tamenori, T. Ohta, and Y. Uchimoto, *Chem. Mater.*, **32**, 139 (2020).
19. W.-S. Yoon, M. Balasubramanian, K. Y. Chung, X.-Q. Yang, J. McBreen, C. P. Grey, and D. A. Fischer, *J. Am. Chem. Soc.*, **127**, 17479 (2005).
20. H. Hafiz, K. Suzuki, B. Barbiellini, N. Tsuji, N. Yabuuchi, K. Yamamoto, Y. Orikasa, Y. Uchimoto, Y. Sakurai, H. Sakurai, A. Bansil, and V. Viswanathan, *Nature*, **594**, 213 (2021).
21. K. Luo, M. R. Roberts, R. Hao, N. Guerrini, D. M. Pickup, Y.-S. Liu, K. Edstrom, J. Guo, A. V. Chadwick, L. C. Duda, and P. G. Bruce, *Nat. Chem.*, **8**, 684 (2016).
22. A. Watanabe, K. Yamamoto, T. Uchiyama, T. Matsunaga, A. Hayashi, K. Maeda, H. Kageyama, and Y. Uchimoto, *ACS Appl. Energy Mater.*, **3**, 4162 (2020).
23. M. A. Reddy and M. Fichtner, *J. Mater. Chem.*, **21**, 17059 (2011).
24. D. Zhang, H. Nakano, K. Yamamoto, K. Tanaka, T. Yahara, K. Imai, T. Mori, H. Miki, S. Nakanishi, H. Iba, T. Watanabe, T. Uchiyama, K. Amezawa, and Y. Uchimoto, *ACS Appl. Mater. Interfaces*, **13**, 30198 (2021).
25. D. Zhang, K. Yamamoto, A. Ochi, Y. Wang, T. Yoshinari, K. Nakanishi, H. Nakano, H. Miki, S. Nakanishi, H. Iba, T. Uchiyama, T. Watanabe, Y. Orikasa, K. Amezawa, and Y. Uchimoto, *J. Mater. Chem. A*, **9**, 406 (2021).
26. T. Yoshinari, D. Zhang, K. Yamamoto, Y. Kitaguchi, A. Ochi, K. Nakanishi, H. Miki, S. Nakanishi, H. Iba, T. Uchiyama, T. Watanabe, T. Matsunaga, K. Amezawa, and Y. Uchimoto, *J. Mater. Chem. A*, **9**, 7018 (2021).
27. D. Zhang, T. Yoshinari, K. Yamamoto, Y. Kitaguchi, A. Ochi, K. Nakanishi, H. Miki, S. Nakanishi, H. Iba, T. Watanabe, T. Uchiyama, Y. Orikasa, K. Amezawa, and Y. Uchimoto, *ACS Appl. Energy Mater.*, **4**, 3352 (2021).
28. D. Zhang, K. Yamamoto, Y. Wang, S. Gao, T. Uchiyama, T. Watanabe, T. Takami, T. Matsunaga, K. Nakanishi, H. Miki, H. Iba, K. Amezawa, K. Maeda, H. Kageyama, and Y. Uchimoto, *Adv. Energy Mater.*, **11**, 2102285 (2021).
29. Y. Zhu and C. Wang, *J. Phys. Chem. C*, **114**, 2830 (2010).
30. D. Aurbach, M. D. Levi, E. Levi, H. Teller, B. Markovsky, G. Salitra, U. Heider, and L. Heider, *J. Electrochem. Soc.*, **145**, 3024 (1998).
31. J. Xie, N. Imanishi, T. Zhang, A. Hirano, Y. Takeda, and O. Yamamoto, *Electrochim. Acta*, **54**, 4631 (2009).
32. H. Xia, L. Lu, and G. Ceder, *J. Power Sources*, **159**, 1422 (2006).
33. J. Xie, K. Kohno, T. Matsumura, N. Imanishi, A. Hirano, Y. Takeda, and O. Yamamoto, *Electrochim. Acta*, **54**, 376 (2008).
34. M. A. Nowroozi, K. Wissel, M. Donzelli, N. Hosseinpourkahvaz, S. Plana-Ruiz, U. Kolb, R. Schoch, M. Bauer, A. M. Malik, J. Rohrer, S. Ivlev, F. Kraus, and O. Clemens, *Commun. Mater.*, **1**, 27 (2020).
35. Y. Wang, K. Yamamoto, Y. Tsujimoto, T. Matsunaga, D. Zhang, Z. Cao, K. Nakanishi, T. Uchiyama, T. Watanabe, T. Takami, H. Miki, H. Iba, K. Maeda, H. Kageyama, and Y. Uchimoto, *Chem. Mater.*, **34**, 609 (2022).